A binding site for phosphoinositides described by multiscale simulations explains their modulation of voltage gated sodium channels

Yiechang Lin*, Elaine Tao*, James P Champion, Ben Corry

Research School of Biology, Australian National University, Canberra.

**These authors contributed equally.*

Corresponding authors: Yiechang Lin, Elaine Tao, Ben Corry

Email: yiechang.lin@anu.edu.au, elaine.tao@anu.edu.au, ben.corry@anu.edu.au

Author Contributions: YL, ET and JC performed the research and analyzed the data. YL, ET and BC designed the research and wrote the paper.

Authors declare no competing interests.

Classification: Biological Sciences/ Biophysics and Computational Biology

Keywords: sodium channels, phosphoinositide, molecular dynamics

This PDF file includes:

Main Text
Figures 1 to 7

Abstract

Voltage gated sodium channels (Na_v) are membrane proteins which open to facilitate the inward flux of sodium ions into excitable cells. In response to stimuli, Na_v channels transition from the resting, closed state to an open, conductive state, before rapidly inactivating. Dysregulation of this functional cycle due to mutations causes diseases including epilepsy, pain conditions and cardiac disorders, making Na_v channels a significant pharmacological target. Phosphoinositides are important lipid cofactors for ion channel function. The phosphoinositide $PI(4,5)P_2$ decreases $Na_v1.4$ activity by increasing the difficulty of channel opening, accelerating fast inactivation and slowing recovery from fast inactivation. Using multiscale molecular dynamics simulations, we show that $PI(4,5)P_2$ binds stably to inactivated Na_v at a conserved site within the DIV S4-S5 linker, which couples the voltage sensing domain (VSD) to the pore. As the Na_v C-terminal domain is proposed to also bind here during recovery from inactivation, we hypothesise that $PI(4,5)P_2$ prolongs inactivation by competitively binding to this site. In atomistic simulations, $PI(4,5)P_2$ reduces the mobility of both the DIV S4-S5 linker and the DIII-IV linker, responsible for fast inactivation, slowing the conformational changes required for the channel to recover to the resting state. We further show that in a resting state Na_v model, phosphoinositides bind to VSD gating charges, which may anchor them and impede VSD activation. Our results provide a mechanism by which phosphoinositides alter the voltage dependence of activation and the rate of recovery from inactivation, an important step for the development of novel therapies to treat Na_v-related diseases.

Significance

Voltage-gated sodium channels form pores in the membrane to mediate electrical activity in nerve and muscle cells. They play critical roles throughout the human body and their dysfunction leads to diseases including epilepsy, cardiac arrhythmias and pain disorders. Membrane lipids called phosphoinositides have recently been shown to reduce the activity of a voltage-gated sodium channel, but the molecular basis of this mechanism is not known. Here we use simulations to reveal where these lipids bind to the channels and how they reduce channel activity by making it harder for the pores to open and slower to subsequently recover to the closed resting state.

Introduction

Voltage-gated sodium (Na_v) channels are critical to the regulation of brain activity, cardiac rhythm, and muscle contraction. Expressed in the membranes of excitable cells, Na_v channels respond to membrane depolarization to open a pore that facilitates the selective flow of sodium current into the cell, initiating the action potential. In mammals, the Na_v channel family consists of nine subtypes (Na_v 1.1-1.9), distributed throughout the central and peripheral nervous system, as well as in cardiac and skeletal muscle (1). The $Na_v1.4$ subtype is predominantly expressed in skeletal myofibers, where it initiates muscle contraction. Genetic mutations in this subtype are associated with various motor dysfunctions, such as both hyperkalaemic and hypokalaemic periodic paralyses (2-4). $Na_v1.7$ is found in peripheral sensory neurons and is responsible for nociception. Several pain disorders, such as inherited erythromelalgia and small fibre neuropathy arise from gain-of-function $Na_v1.7$ mutations (5). Both Na_v subtypes have been investigated as promising pharmacological targets for the treatment of myopathy and pain conditions (5, 6).

Structurally, Na_v channels consist of four homologous domains (DI-DIV) arranged in a domain-swapped configuration (Fig. 1A-B). Each domain comprises of six transmembrane helices (S1-S6). The central pore domain is formed by S5, S6 helices and selectivity filter (SF), while the four peripheral voltage-sensing domains (VSDs) are formed by S1-S4 (7, 8). The pore domain also features lateral fenestrations that provide a pathway for the access of small molecules to the pore via the membrane (9) and have been

shown in computational studies to be accessible to lipid tails (10-13). Additionally, the C-terminal domain (CTD) extends from the DIV S6 helix into the cytoplasm, where it is thought to associate with the DIII-IV and DIV S4-S5 linkers in the resting state (14).

Na_v channels adopt distinct functional states during the cycle of membrane depolarization and repolarization (Fig. 1C). In the resting state, the pore is closed and VSD S4 helices are in the down, deactivated state. Membrane depolarization triggers the asynchronous transition of VSD I-III S4 helices to the up, activated conformation, causing Na_v channels to open (15-17). During prolonged depolarization, VSD-IV moves upwards, causing the channels to adopt a fast inactivated state in which a three-residue Ile-Phe-Met (IFM) hydrophobic motif located on the intracellular linker between DIII and DIV (DIII-IV linker) allosterically closes the pore (18). The CTD is proposed to bind at the S4-S5 linker of VSD-IV and sequester the DIII-IV linker during the resting state. During fast inactivation, the CTD dissociates from VSD-IV and releases the DIII-IV linker to allow IFM binding (14). Upon repolarization, the VSDs deactivate, the IFM motif disassociates, the CTD rebinds to VSD-IV and the pore returns to the resting state.

Phosphoinositides (PIPs) are important cellular signaling molecules found on the cytoplasmic leaflet of the mammalian cell membrane. They can exist in seven forms, with phosphorylation possible at one (PIP1), two (PIP2) or all three (PIP3) positions on the inositol ring, at the 3', 4' and/or 5' carbons. PIPs, particularly $PI(4,5)P_2$, featuring phosphates at the 4' and 5' carbon positions (Fig. 1D), are known to bind and modulate the activity of numerous ion channels families (19). These include voltage-gated ion channels, some of which have been resolved with $PI(4,5)P_2$ bound (20, 21). PIP is known to interact with the VSDs of different potassium channels, to stabilize the positive gating charges and support the voltage-sensing mechanism (22). By also binding at the VSD-pore interface in channels such as $K_v7.1$, PIP is proposed to facilitate coupling of VSD movement to pore opening (20, 23, 24). $PI(4,5)P_2$ also forms specific interactions with VSD-II of $Ca_v2.2$ in the down-state, making channel activation more difficult (21). Although $PI(4,5)P_2$ is known to bind to numerous voltage gated ion channels, its effects on channel gating and function are complex and yet to be fully elucidated.

Recent experiments show that $Na_v1.4$ channel kinetics and voltage dependence are modulated by $PI(4,5)P_2$ (25). $PI(4,5)P_2$ inhibits $Na_v1.4$ by causing a depolarizing shift in voltage dependence of activation, accelerating transition to the inactivated state and slowing recovery from inactivation, resulting in reduced peak current and suppression of late current (summarized in Fig. 1C). While this is likely to occur via a direct interaction with $Na_v1.4$, the structural basis of $PI(4,5)P_2$ modulation remains to be understood.

Here, we used a combination of coarse-grained and atomistic MD simulations to identify a putative PIP binding site to inactivated $Na_v1.4$ in VSD-IV and the DIII-IV linker. We analyze the atomistic level interactions between the positively charged residues at this site with $PI(4,5)P_2$ and PI(4)P, comparing this with structurally resolved PIP binding sites in the related ion channels $Ca_v2.2$ and $K_v7.1$. Consistent with the sequence conservation at the identified site, we find that PIPs also bind to $Na_v1.7$ in coarse-grained simulations, with notable differences dependent on VSD conformation states. This work provides insight into how PIPs can negatively regulate Na_v channels, a first step for the potential development of PIP-analogue sodium channel inhibitors.

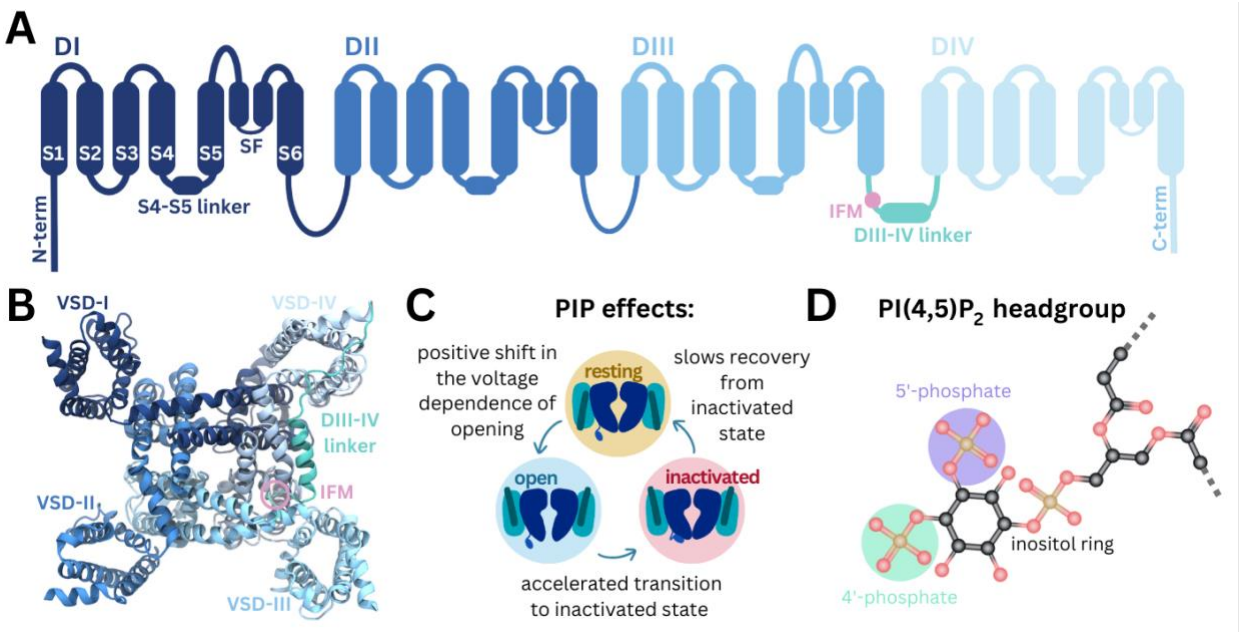

Fig. 1 Structure of Na_v and modulation by phosphoinositides (A) Na_v channel topology featuring transmembrane helices (S1-S6), the selectivity filter (SF) and the DIII-IV linker (containing the IFM motif) located between DIII and DIV. **(B)** $Na_v1.4$ structure (6agf) showing the four domain-swapped voltage sensor domains (VSDs I-IV), pore and DIII-IV linker on the intracellular side. **(C)** Summary of $PI(4,5)P_2$ effects on transitions between Na_v channel functional states (25) **(D)** Structure of the $PI(4,5)P_2$ headgroup with the 4'- and 5'- phosphates indicated

Results

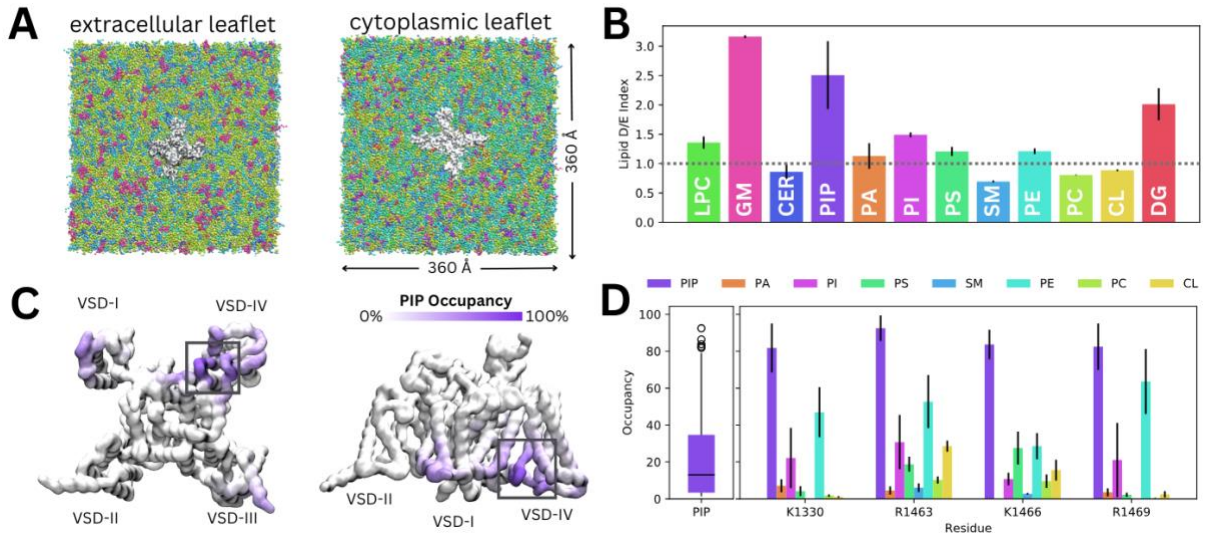

Fig. 2 Lipid fingerprint and binding of all PIP types to $Na_v1.4$ (A) $Na_v1.4$ embedded in a 360 Å x 360 Å model mammalian membrane containing 63 lipid species. **(B)** Lipid depletion enrichment index of lipids around $Na_v1.4$ grouped into 12 headgroup classes **(C)** $Na_v1.4$, shown from the intracellular (left) and membrane (right) sides, colored by PIP occupancy (darker purple = greater PIP occupancy) **(D)** Distribution of PIP binding occupancies (left) and occupancy of lipid species at 4 residues with the highest PIP occupancy.

To investigate how diverse lipid species interact with $Na_v1.4$, we carried out coarse-grained simulations of $Na_v1.4$ (PDB ID: 6agf, inactivated state) embedded in a complex mammalian membrane for 16 µs in triplicate (Fig. 2A). Glycosphingolipid (GM), phosphoinositide (PIP) and diacylglycerol (DAG) were highly enriched around $Na_v1.4$ (Fig. 2B). Additionally, we observed modest enrichment of lysophosphatidylcholine (LPC), phosphatidylinositol (PI), phosphatidylserine (PS) and phosphatidylethanolamine (PE) and slight depletion of ceramide (CER), sphingomyelin (SM), phosphatidylcholine (PC) and cholesterol (CL). To investigate specific interactions, we generated z-density maps and calculated the per-residue occupancy of the 12 different lipid types (Fig. 2C, Fig. S1-2). Binding residues of interest were identified by constructing occupancy distributions by residue for each lipid type and identifying outlying values with high occupancies (Fig. S3). DG lipids form significant interactions within the lateral fenestrations of $Na_v1.4$ (Fig. S2). LPC and PI also frequently interact with different VSD residues (Fig. S1).

Given our interest in understanding the modulation of $Na_v1.4$ by PIPs, we focus on their interactions for the remainder of this manuscript. Despite the very low concentration of PIPs (0.5% each of PIP1, PIP2 and PIP3) in the mammalian membrane, they are highly enriched around $Na_v1.4$, particularly near the DIII-IV linker and the VSD-IV (Fig. 2C). Contact analysis revealed a putative PIP binding site involving the K1330 residue of the DIII-IV linker and residues R1463, K1466 and R1469 in the DIV S4-S5 linker, which connects the pore and VSD-IV (Fig. 2D). Across all three replicates, only residues within this site were occupied by PIPs for more than 80% (Quartile 3 + 1.5 x Interquartile range) of simulation time on average (Fig. 2D). We note that these residues have higher occupancies for PIP compared to other lipids, including other negatively charged phospholipids (PA, PS and PI) (Fig. 2D).

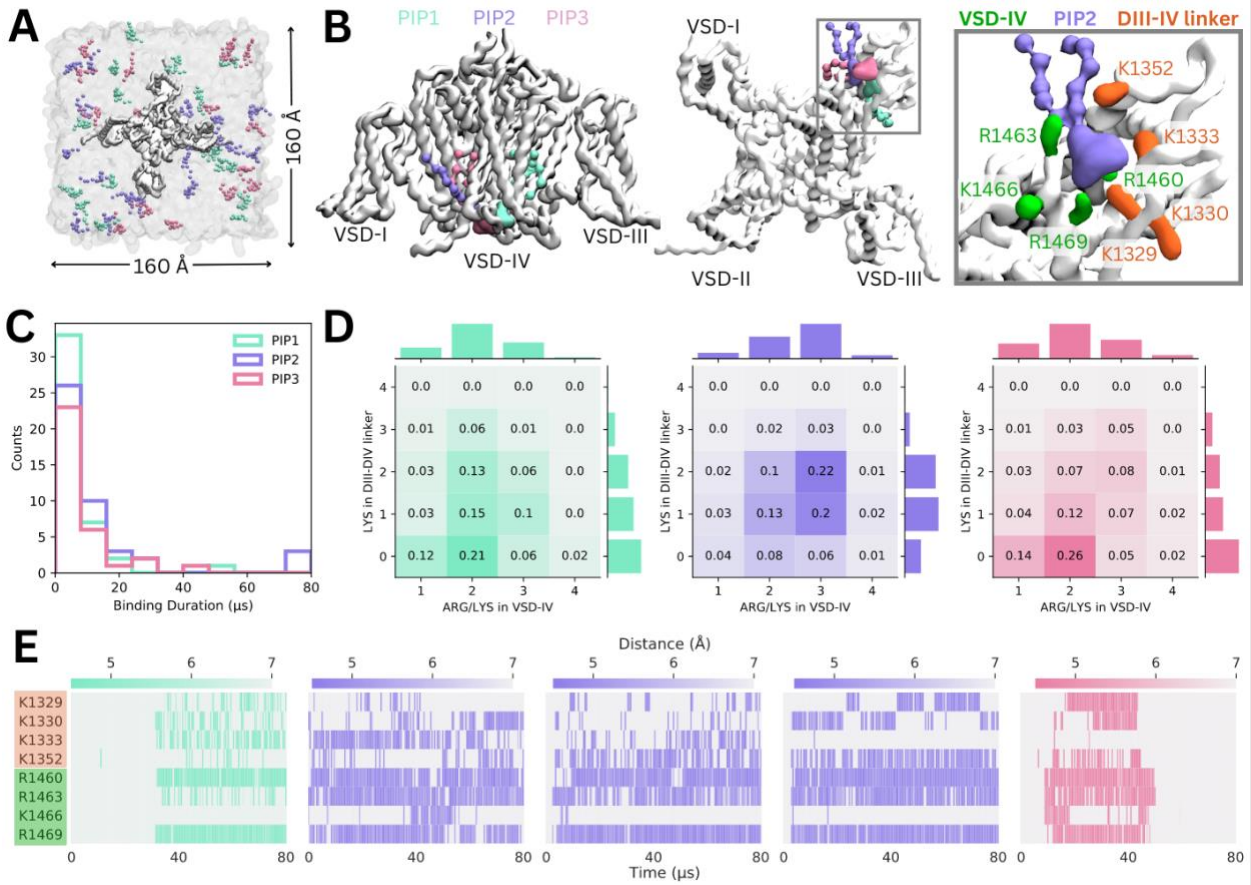

Fig. 3 Binding of different PIP species in enriched PIP simulations (A) Enriched PIP simulation system, with $Na_v1.4$ embedded in a POPC membrane (transparent gray) and 5% each of PIP1 (blue), PIP2 (purple) and PIP3 (pink) added to the cytoplasmic leaflet. **(B)** Representative snapshots from the five longest binding events from different replicates, showing the three different PIP species (PIP1 in blue, PIP2 in purple and PIP3 in pink) binding to VSD-IV and the DIII-IV linker. $Na_v1.4$ is shown in white with interacting residues on the DIV S4-S5 linker and the DIII-IV linker colored in green and orange respectively. **(C)** A frequency distribution showing interaction times for each PIP species, defined as the length of a continuous period in which a PIP was within 0.7 nm of two VSD IV binding site residues. **(D)** Frequency plots showing number of positive residues interacting with bound PIP in the DIII-IV linker (vertical) and VSD-IV (horizontal). **(E)** Minimum distance between binding residues on $Na_v1.4$ and bound PIPs lipid across simulation time for the five longest binding events, colored by distance and the type of PIP bound.

Simulations in a complex mammalian membrane showed that PIP species bind specifically and selectively to $Na_v1.4$ in the presence of other negatively charged lipids and at low, physiological concentrations. However, the large membrane required, and long PIP binding durations prevented sampling of large numbers of binding and unbinding events. To address this, we carried out additional simulations where $Na_v1.4$ was placed in a smaller POPC membrane with a 5% concentration of each PIP species in the cytoplasmic leaflet (Fig. 3A).

Across ten replicates of these enriched PIP simulations, each carried out for 80 μs, we observed all three PIP species binding at the identified site on VSD-IV and DIII-IV linker (Fig. 3B). PIPs can approach and bind to this site from either side of the VSD, however, PIP1 only forms stable interactions when it approaches and binds from the VSD-I side while PIP2 and PIP3 usually bind from the VSD-III side (Fig.

3B). These enriched PIP simulations also revealed additional positively charged residues in the DIII-IV linker (K1329, K1333 and K1352) and DIV S4 (R1460) which support binding.

There were 156 PIP binding/unbinding events with duration greater than 2 µs occurring in the identified site (Fig. 3C). Of these, 43 were with PIP1, 44 with PIP2 and 33 with PIP3. The number of short-term (2-10 µs) interactions decreased with headgroup charge. That is, PIP1 formed the greatest number of short-term interactions while PIP3 had the fewest. Of the 31 binding events with duration greater than 10 µs, 7 were with PIP1, 15 with PIP2 and 9 with PIP3 (Fig. S4-5).

When we analyzed interactions occurring during 2-80+ µs binding events, we found that the number of interacting basic residues changes depending on the PIP headgroup charge (Fig. 3D). PIP1 (headgroup charge: -3e) binding is most frequently coordinated by two positive charges in VSD-IV and zero or one residue in the DIII-IV linker. PIP2 (headgroup charge: -5e) binding most frequently involves one or two interactions from the DIII-IV linker and three from VSD-IV for a total of five interactions. Interestingly, despite its greater negative charge, PIP3 (headgroup charge: -7e) interacts similarly to PIP1, and has fewer interactions than PIP2.

The minimum distance between the interacting PIP headgroup and each binding residue across simulation time is shown for the five 40+ µs PIP binding events (Fig. 3E). Of these, three are PIP2 binding events which almost span the entire 80 µs of simulation. One 40+ µs binding event each for PIP1 and PIP3 were also observed. The stable PIP1 binding event observed involved interactions with R1460 and R1469 in VSD-IV, as well as fluctuating interactions with the four residues of the DIII-IV linker (K1329, K1330, K1333, K1352). The three long term PIP2 binding events observed were similar to each other, mainly stabilized by R1460, R1463 and R1469. As with PIP1, the number and identity of interacting DIII-IV linker residues varied across the span of each simulation and between replicates, owing to the flexibility of the linker. Like PIP2, PIP3 binding was characterized by stable interactions with R1460, R1463 and R1469 (VSD-IV) as well as K1329 and K1330 (DIII-IV linker). *In silico* mutation of the eight residues implicated in PIP binding to leucine (charge neutralization while preserving sidechain size) or glutamate (charge reversal) significantly reduced PIP binding (Fig. S6).

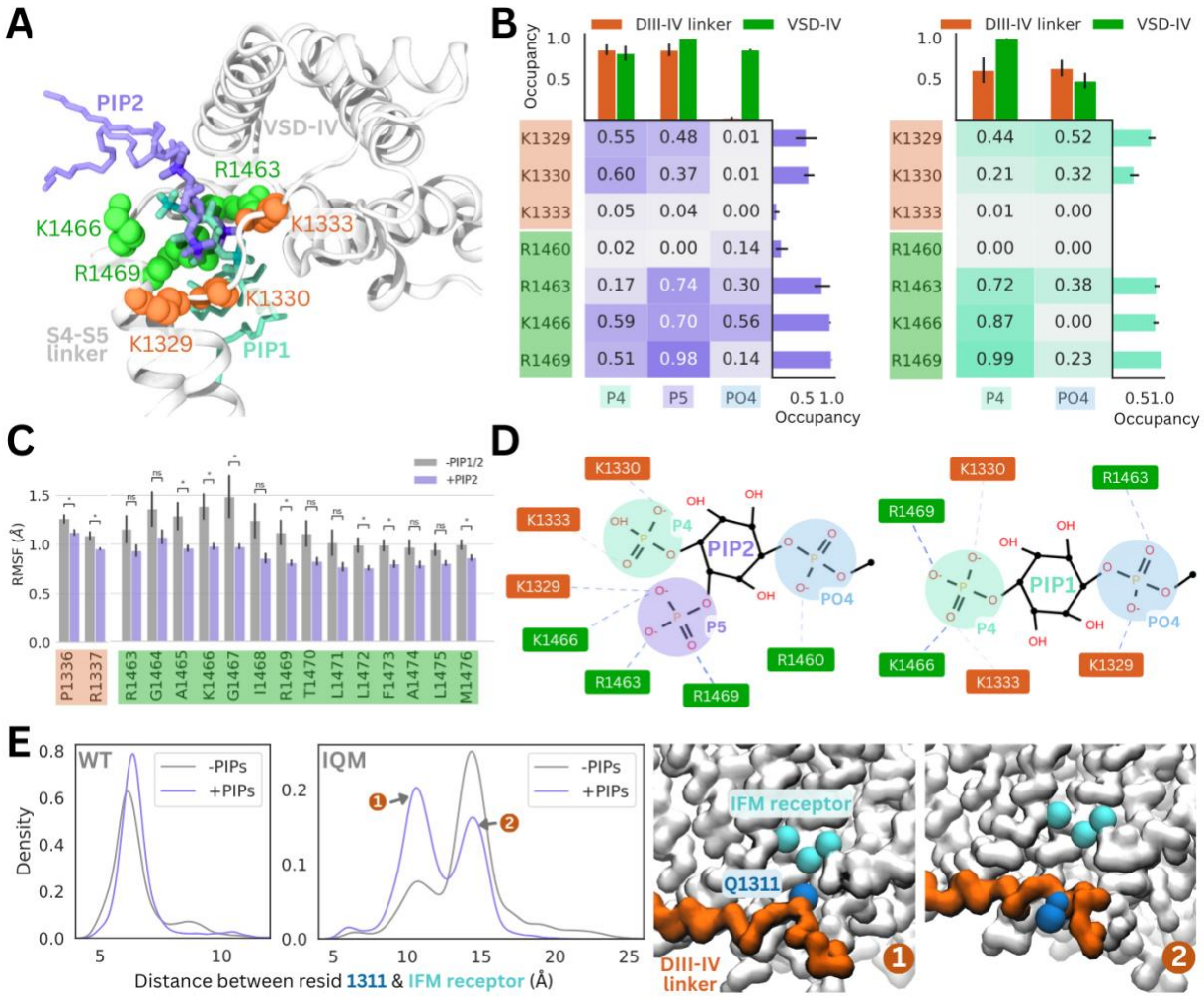

Fig. 4 PI(4,5)P_2 and PI(4)P binding to $Na_v1.4$ stabilizes the DIII-IV linker in atomistic and flexible coarse-grained simulations (A) Representative snapshots of PI(4,5)P_2 bound from the VSD-I side (purple stick) and PI(4)P bound from the VSD-III side (cyan stick), with six basic residues forming the binding site located on the DIII-IV linker (orange VDW representation) and VSD-IV S4-S5 linker (shown in green VDW representation) visualized from the intracellular face of the protein **(B)** Proportion of frames where each of the binding site residues were identified to be within 4.5 Å with the different headgroup regions, P4, P5 and PO4, for PI(4,5)P_2 (left) and PI(4)P (right) **(C)** Comparison of RMSF per carbon-alpha for simulations with and without bound PI(4,5)P_2, showing residues on the S4-S5 linker and DIV linker with significant differences in mobility (p-value < 0.05) **(D)** Interaction network plots between the PIP headgroup and basic binding residues on DIII-IV linker (orange) and DIV S4-S5 linker (green), generated by ProLIF – showing the dominant interactions across simulations of PI(4,5)P_2 and PI(4)P. **(E)** Density plots showing differences in the distributions of distance between IFM/IQM motif and its binding pocket in the presence and absence of PIPs for the Nav1.4 wild-type (left) and IFM->IQM mutant (right); with representative snapshots showing the two distinct conformations of the IQM motif in the mutant.

Coarse-grained simulations enhance sampling by reducing the number of particles, enabling larger time steps and construction of a smoother energy surface. To examine interactions and protein conformational changes in atomistic detail, we backmapped representative snapshots from our PIP enriched simulations, where we observed stable, long-term binding events between $Na_v1.4$ and PIP1/PIP2. The coarse-grained

PIP1 and PIP2 molecules were converted to the atomistic PI(4)P and PI(4,5)P_2 respectively. For each system, 7.5 µs of atomistic simulations were performed (5 replicates, 1.5 µs each).

In these simulations, the PI(4,5)P_2 headgroup was stable at the binding site identified in coarse-grain simulations (RMSD <2.2 Å) (Fig. 4A, Fig. S7). PI(4,5)P_2 binding is predominantly coordinated by R1469 on the DIV S4-S5 linker, as well as R1466 and R1463. In one replicate, PI(4,5)P_2 associates with R1460 via the phosphate group (PO4) that connects the headgroup to the PIP tails. The PI(4,5)P_2 headgroup also forms electrostatic interactions with K1329 and K1330 in the DIII-IV linker, but forms few contacts with K1333 (Fig. 4B, Fig. S8). This loop portion of the DIII-IV linker is highly flexible (Fig. S7), thus the lysine sidechains are able to flip between binding the PI(4,5)P_2 headgroup and facing the intracellular space.

The 4'-phosphate formed interactions with residues belonging to the DIII-IV linker (K1329 and K1333) and DIV S4-S5 linker (K1666 and R1469) with similar frequency, in 55-60% of simulation frames (Fig. 4B). In contrast, the 5'-phosphate formed contacts with three VSD-IV S4-S5 residues (R1463, K1466 and R1469) in 70-98% of simulation frames and DIII-IV linker residues in 37-48% of frames. Taken together, this data suggests that although the headgroup is flexible when bound, the 5'-phosphate is more important for coordinating VSD-IV S4-S5 residues while the 4'-phosphate associates with both regions of the binding site.

Atomistic simulations of PI(4)P bound from the VSD-III side show that this is also a stable pose (RMSD <2 Å), where the headgroup interacts with the same positively charged residues as seen for PI(4,5)P_2 (Fig. 4A, Fig. S7). The residues on the S4-S5 linker, R1463, K1466 and R1469, predominantly bind to the 4'-phosphate (Fig. 4B). Due to the more buried location of PI(4)P binding, the PO4 phosphate can associate more with DIII-IV linker lysines (Fig. 4B), however, the absence of the 5'-phosphate leads to a reduced number of total electrostatic interactions (Fig. S9).

To investigate structural changes that might occur in the presence of PI(4)P/PI(4,5)P_2, we also carried out simulations of the inactivated Na_v1.4 structure without any PIPs bound for comparison. Although the DIII-IV linker remains bound throughout simulations both with and without PIPs, residues P1336 and R1337 in the DIII-IV linker downstream of the IFM motif are significantly less mobile with PI(4,5)P_2 present (Fig. 4C). Additionally, seven residues belonging to the DIV S4-S5 linker, including binding residues K1466 and R1469, also have significantly lower mobility when PI(4,5)P_2 is bound (Fig. 4C). In the PI(4)P bound simulations, there were no significant differences in DIII-IV linker or S4-S5 linker mobility.

To further probe whether PIP can stabilize the DIII-IV linker and the inactivation gate, we applied coarse-grained simulations with the DIII-IV linker unrestrained. In simulations of WT Nav1.4, the IFM has a reduced stability within its binding pocket when PIP is excluded from the membrane (Fig. 4E). To accentuate this effect we simulated an inactivation-deficient variant of Nav1.4, where the IFM motif is mutated to IQM (26). We find that the IQM motif has a greater probability of being tightly associated with the receptor pocket in the presence of PIP compared to without it (Fig. 4E), supporting our observation that PIP can stabilize the channel in the inactivated state. This suggests that the presence of PIP may partially rescue some of the structural defects associated with inactivation dysfunction in Nav mutants.

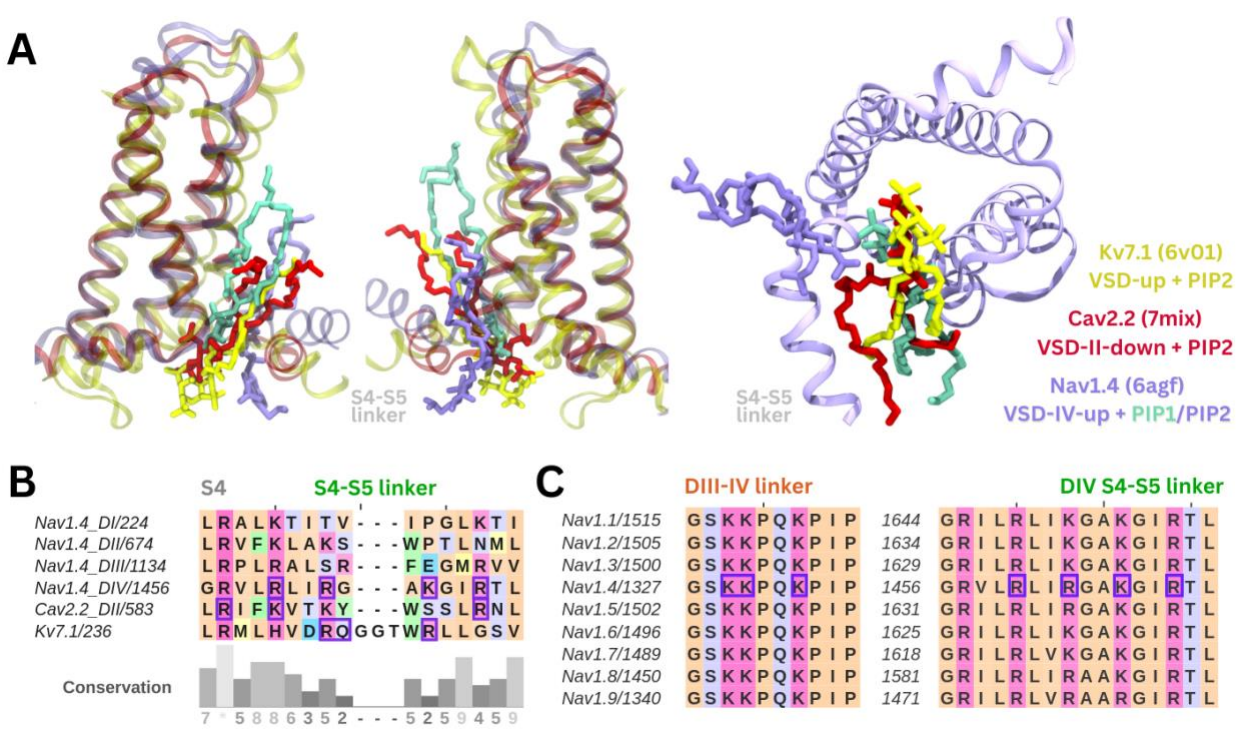

Fig. 5 Comparison of the identified phosphoinositide binding site to Na_v subtypes and other ion channels (A) Binding poses of $PI(4,5)P_2$ (in purple) and PI(4)P (in cyan) aligned with two other tetrameric channels structures $K_v7.1$ (6v01, in yellow) and $Ca_v2.2$ (7mix, in red) that were resolved with $PI(4,5)P_2$ at their respective VSDs. **(B)** Sequence alignment of the S4 helix and S4-S5 linker of the four domains of $Na_v1.4$, compared to VSD-II of $Ca_v2.2$ and one of the four identical VSDs of $K_v7.1$; residues colored by amino acid class; purple boxes indicate $PI(4,5)P_2$ binding residues (identified with 5 Å of the headgroup). **(C)** Sequence alignment of the nine human Na_v channel subtypes shows high sequence similarity in the S4 helix, S4-S5 linker and DIII-IV linker regions.

The PIP binding poses seen in our simulations is similar to resolved binding poses for $PI(4,5)P_2$ in cryo-EM structures of $Ca_v2.2$ and $K_v7.1$ (Fig. 5A). A sequence alignment of $Na_v1.4$ VSDs show that there are more positively charged residues present in the S4/S4-S5 linker regions of DIV compared to the other domains (Fig. 5B). PIP is bound at similar VSD residues on both these ion channels, with PIP forming interactions with a gating charge further up the S4 helix in $Ca_v2.2$ due to the VSD being in a different state. Additionally, the high sequence similarity in the S4/S5-S5 linker and DIII-IV linker regions between the nine human Na_v channel subtypes suggests conservation of the PIP binding site (Fig. 5C).

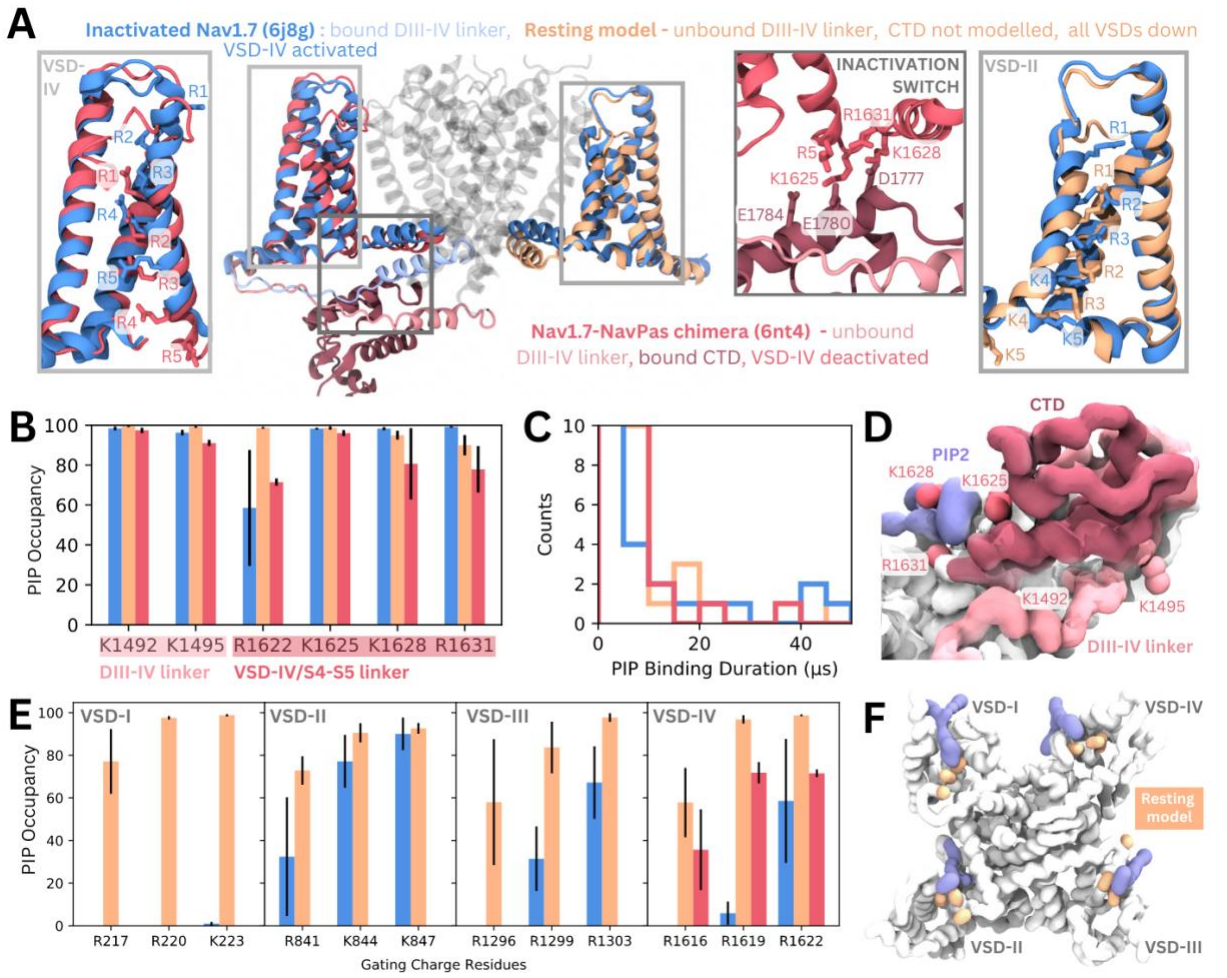

Fig. 6 PIP binding to $Na_v1.7$ with different VSD states in coarse-grained simulations (A) Atomistic representation of the three different $Na_v1.7$ structures simulated: (1) the inactivated state (blue, PDB ID: 6j8g) with the VSDs all in the activated, up state (2) the $Na_v1.7$-Na_vPas chimera (pink, PDB ID: 6nt4) with the $Na_v1.7$ VSD-IV in the deactivated, down state and a bound Na_vPas CTD (3) a $Na_v1.7$ resting state model (orange, model generation detailed in Table. S2) with all four VSDs in the deactivated, down state. Panel insets show the different conformations of VSD-IV (left) and VSD-II (right) across different structures. The inactivation switch formed by the CTD and VSD-IV S4-S5 linker proposed by Clairfeuille et al. is shown (middle). **(B)** Combined occupancy of all PIP species (PIP1, PIP2, PIP3) at binding site residues in the three systems **(C)** Distribution of PIP binding durations at the identified site **(D)** Intracellular view of CTD covering the resting state VSD-IV. Representative snapshot of PIP binding at DIV S4-S5 linker in the $Na_v1.7$-Na_vPas system. The CTD (dark pink) prevents PIP access to DIII-IV linker lysines, K1492 and K1495. **(E)** Combined PIP occupancy at the bottom three gating charges on VSD I-III in the inactivated (blue) and resting state model (orange) simulations. For VSD-IV, PIP occupancy in the $Na_v1.7$-Na_vPas system (pink) is also shown. **(F)** Representative simulation snapshot showing PIP (purple) binding at the gating charges (orange) in the resting state model simulations.

To assess possible state- and subtype-dependent differences in PIP binding, we simulated three structures of $Na_v1.7$ with different VSD conformations in a PIP enriched membrane (Fig. 6A). The inactivated $Na_v1.7$ structure (blue, PDB ID: 6j8g) contains all VSDs in the activated/up state and a bound DIII-IV linker. We also simulated a Na_vPas (American cockroach) chimera structure with a human $Na_v1.7$ VSD-IV in the deactivated/down state (VSDs I-III are activated, and from Na_vPas) (pink, PDB ID: 6nt4). This structure (14) features a dissociated DIII-IV linker and a resolved C-terminal domain bound to the DIV S4-S5 linker

(forming the 'inactivation switch') at residues identified to form part of our PIP binding site. To assess PIP binding at VSD I-III in the deactivated/down state, we modelled the $Na_v1.7$ resting state based on templates structures in which different VSDs have been captured in deactivated states with the aid of toxins (detailed in Table S2). These structures feature three or more of the gating charge residues below the hydrophobic constriction site (HCS) and displacement of the S4-S5 linker (Fig. S10). Given that no resting state mammalian Na_v channel structure has been resolved, it is possible that the modelled VSDs may not reflect the fully deactivated state.

In triplicate 50 µs coarse-grained simulations, PIPs bind to the analogous site to that seen in inactivated $Na_v1.4$ in the inactivated $Na_v1.7$ structure, interacting with residues belonging to both the DIII-IV linker and VSD-IV for durations comparable to $Na_v1.4$, (Fig. 6B-C, Fig. S11). Binding of PIP to the DIV S4-S5 linker to the deactivated VSD-IV in the $Na_v1.7$-Na_vPas chimera and resting state model was also observed (Fig. 6B-C). However, in the $Na_v1.7$-Na_vPas chimera, the PIP bound at the S4-S5 linker cannot simultaneously associate with the DIII-IV linker (Fig. S11), due to its sequestration by the C-terminal domain, which moves the lysines away from the binding VSD-IV residues (Fig. 6D). Instead, K1491, K1492 and K1495 (on the DIII-IV linker) are occupied by different PIPs on the other side of the VSD. In the resting state model, which features an unbound DIII-IV linker PIPs binding at the DIV S4-S5 residues also do not associate with the DIII-IV linker (Fig. S11). Comparison of binding durations at this site across the three systems reveals a greater number of long PIP interactions (> 20 µs) with inactivated $Na_v1.7$ (5) compared to $Na_v1.7$-Na_vPas (3) or the resting state model (2) where VSD-IV is down, and the DIII-IV linker is dissociated.

There are state-dependent differences in PIP occupancy at the gating charges in each VSD (Fig. 6E-F, Fig. S12A-B). PIP can associate with the lowest three gating charges VSD-I of the resting state model, but not in the inactivated state (Fig. 6E). This is likely due to the large displacement in the DI-S4 helix, which moves down three helical turns in the resting state model so that all gating charges are below the HCS (Fig. S10). In VSD II and III, the PIP interaction differences between inactivated and resting state are present but less pronounced, owing to a smaller difference in the relative displacement between the gating charges between states (Fig. S10). PIP occupancy is also higher at VSD-IV when it is in the deactivated conformation however, the presence of a bound CTD as seen in the $Na_v1.7$-Na_vPas model, reduces this occupancy of PIP (Figure 6E). Additional simulations of a resting state model of Nav1.4 built using our Nav1.7 resting state model as a template suggest that similar gating charge interactions occur for Nav1.4 when the VSDs are deactivated (Fig. S12C).

Discussion

Recently, $PI(4,5)P_2$ was shown to be a negative regulator of $Na_v1.4$, modulating channel kinetics and voltage dependence. Presence of $PI(4,5)P_2$ causes a depolarizing shift in the voltage dependence of activation, that is a stronger stimulus is required to produce $Na_v1.4$ opening. Additionally, it stabilizes the inactivated state of $Na_v1.4$, marked by both shortened times to inactivation and slowed recovery from the inactivation.

Using a multiscale simulation approach, we identified a putative PIP binding site comprised of positively charged residues belonging to the S4 helix/S4-S5 linker of VSD-IV (R1460, R1463, K1466, R1469) and DIII-IV linker (K1329, K1330, K1333, K1352). Coarse grained simulations of $Na_v1.4$ embedded in a complex membrane showed that PIP interacts with residues belonging to VSD-IV and the DIII-IV linker. In coarse grained enriched PIP simulations, PIP2 formed longer duration interactions with $Na_v1.4$ than PIP1 and PIP3, supported by a greater number of charged interactions. Atomistic simulations verified the stability of $PI(4,5)P_2$ (the most common PIP2 species in the plasma membrane) at this site and showed that the binding of $PI(4,5)P_2$ reduces the mobility of some DIV S4-S5 and DIII-IV linker residues. Simulations of $Na_v1.7$ with VSDs in different conformational states showed that the PIP binding site is conserved in $Na_v1.7$ and that PIP interactions at VSD gating charges are functional state dependent, with more interactions being formed when the VSDs are deactivated.

The DIII-IV linker, CTD and S4-S5 linkers all play key roles throughout the Na_v conformational cycle. Mutation of the IFM inactivation motif as well as other residues in the DIII-IV linker alter fast inactivation and recovery from fast inactivation (27, 28). While the precise role of the Na_v C-terminal domain and its conformation during the Na_v activation cycle remain elusive, it is likely to be important for coordinating fast inactivation (14, 29). CTD binding to DIV S4-S5 and sequestration of the DIII-IV linker is proposed to occur in the resting state. After the pore opens, activation of VSD-IV is thought to cause CTD dissociation, releasing the DIII-IV linker to allow fast inactivation. Residues in 'switch 1' of the CTD-binding site on the DIV S4-S5 stably bind PIP in our simulations of inactivated $Na_v1.4$ and $Na_v1.7$. We hypothesize that PIP binding at this location makes it more difficult for the CTD to reassociate with VSD-IV, a conformational change which is required during recovery from inactivation.

More generally, the S4-S5 linkers in all four domains couple the VSD to the pore helices and adopt different orientations depending on VSD activation states. When the VSD is activated (in the open and inactivated states), the S4-S5 linkers lie parallel to the membrane. In the resting state, when the voltage sensor is deactivated, the S4-S5 linkers move downward below the plane of the membrane. We propose that PIP binding at the identified site could additionally stabilize both the DIV S4-S5 linker and DIII-IV linker to favor the inactivated state. Although the recovery from fast inactivation occurs on the order of several milliseconds (30), and is beyond atomistic simulation timescales, we observed statistically significant reductions in the RMSF of several DIII-IV linker and DIV S4-S5 linker residues when $PI(4,5)P_2$ was bound in 1.5 µs atomistic simulations. Reduction in the mobility of the DIII-IV linker may slow the dissociation of the upstream IFM motif and stabilization of the S4-S5 linker prevents the downward movement required for the channel to transition back to the resting state.

The PIP binding residues identified here are conserved in $Na_v1.1$-1.9 (Fig. 5C), suggestive of a shared binding site and mechanism for PIP-mediated modulation across subtypes. Mutations at these conserved residues in other subtypes lead to various gain-of-function diseases (Table S1). For example, analogous to the $Na_v1.4$ R1469 residue, the R1642C mutation (in $Na_v1.3$) leads to developmental epileptic encepahlopathy (31), and R1644C/H mutations in $Na_v1.5$ (analogous to R1469 in $Na_v1.4$) cause cardiac arrythmias, characterized by accelerated rates of channel recovery from inactivation (32). Consistent with our observations, these diseases with mutations on the DIII-IV linker are likely to reduce $PI(4,5)P_2$ binding, which could be a contributing factor to instability of inactivated state in these pathogenic variants. These inactivation-deficient variants, as well as the IQM variant that we simulated, further emphasize that interactions between $PI(4,5)P_2$ with Na_v channels could be important for prolonging the fast-inactivated state.

The PIP binding site identified here harbors sequence and structural similarity to $PI(4,5)P_2$ binding sites found in other cation channels (Fig. 5B). For example, $PI(4,5)P_2$ is resolved at a similar site near the VSD and S4-S5 linker in a recent cryo-EM structure of $K_v7.1$, where the phosphate headgroup forms analogous contacts to R249 and R243 (PDB ID: 6v01) (20). Despite differences in the role of $PI(4,5)P_2$, which negatively regulates $Na_v1.4$ but is required for $K_v7.1$ pore opening, the binding site appears to be conserved. Based on the $PI(4,5)P_2$ binding site, a structurally similar compound was developed as an activator of K_v7 channels and proposed to be a future antiarrhythmic therapy (33).

$PI(4,5)P_2$ also binds to the down, deactivated state of VSD-II in $Ca_v2.2$ (PDB ID: 7mix) (21). In this structure, the $PI(4,5)P_2$ headgroup interacts with two VSD-II gating charges, R584 and K587. Compared to the positioning of $PI(4,5)P_2$ in our simulations of $Na_v1.4$ with an activated VSD-IV, the headgroup associates further up the S4 helix in $Ca_v2.2$ due to the VSD being in a deactivated state. This is also seen in $K_v7.1$ which contains an extended GGT loop in the S4-S5 linker which prevents $PI(4,5)P_2$ binding in the VSD-down state (34). In our coarse-grained simulations of the resting $Na_v1.7$ model, we observe a similar state-dependent difference in $PI(4,5)P_2$ interactions with the deactivated states of each VSD. Since activation of VSDs I-III are known to be coupled to channel opening (17), we propose that PIP binding at these VSDs impedes their ability to activate and thus increases the voltage threshold required of opening. $PI(4,5)P_2$

binding at VSD-IV is prevented by presence of the CTD (and absence of the DIII-IV linker) in the resting state, thus not affecting the kinetics of inactivation onset.

The leftward shift in voltage dependence of inactivation is less pronounced when PI(4,5)P_2 is converted to PI(4)P rather than completely dephosphorylated to PI (25). This suggests that PI(4)P may play a compensatory role when PI(4,5)P_2 is not present. This is supported by our simulations which show that PI(4)P can also stably occupy the identified binding site, albeit with shorter duration and form less electrostatic interactions compared to PI(4,5)P_2. Our atomistic simulations also showed that the 5'-phosphate is more important than the 4'-phosphate for forming interactions with the DIV S4-S5 linker residues of the inactivation switch. These factors suggest that PI(4,5)P_2 binding is preferred over PI(4)P at this site and can better compete to bind over the CTD, implying that PI(4,5)P_2 is more effective at stabilizing the inactivated state and inhibiting recovery to the resting state.

Simulations using the Martini2.2 forcefield have previously been used to investigate lipid-protein interactions (35) and successfully predict specific lipid binding sites, including the PIP binding site on K_{ir} channels (36). While the Martini2.2 PIP species can be parameterized for a specific sub-species (e.g. PI(3,4)P_2 vs PI(4,5)P_2), we instead employed atomistic simulations to complement and strengthen findings from coarse grain simulations, allowing us to identify the specific contribution of the 4'- and 5'-phosphate groups to binding as well as investigate the conformational changes associated with PI(4,5)P_2 binding. Since the precise protonation of the PI(4,5)P_2 headgroup in a physiological setting is unclear, we explore one case with the 4'-phosphate protonated. Given that the PI(4,5)P_2 headgroup can adopt slightly different binding orientations and can fluctuate over the course of atomistic simulations (Fig S8), we expect the alternate protonation state to have similar affinity for the binding site.

In this work we made use of the Martini2.2 model for our coarse-grained simulations, however recently the refined Martini3 (37) has become available and will be a useful tool for further interrogating protein-lipid interactions, as a greater number of lipid parameters become available. Our coarse-grained simulations also allow us to investigate the association of other lipid types with Nav1.4. While we focus on PIP here, there are other lipid species that have modulatory effects on Nav channels, such as cholesterol (38), glycolipids, DG, LPC and PI, and their interactions warrant further investigation.

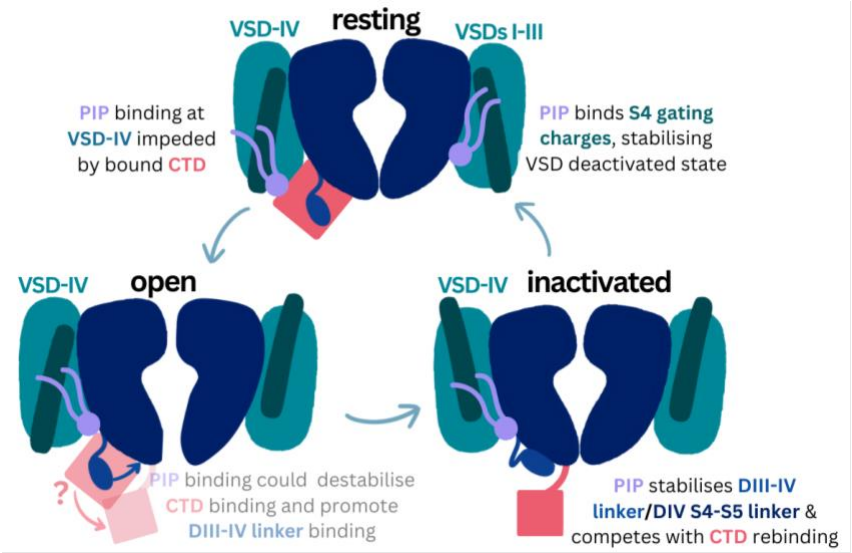

Fig. 7 Proposed mechanism of PIP effects on the sodium channel functional cycle

Conclusion

Using multiscale simulations, we show that PI(4,5)P_2 binds stably to inactivated structures of Na_v1.4 and Na_v1.7 at a conserved site within the DIV S4-S5 linker. As the CTD is proposed to also bind here during recovery from inactivation, we hypothesize that PI(4,5)P_2 competes with the CTD to bind to this site, prolonging inactivation. At this site, PI(4,5)P_2 simultaneously binds to the DIII-IV linker which is responsible for allosterically blocking the pore during fast inactivation (Fig. 7). Its binding reduces the mobility of both the DIV S4-S5 and DIII-IV linkers, potentially slowing the conformational changes required for the channel to recover to the resting state. We also propose that in the resting state, PIPs form additional interactions with S4 gating charges, particularly in VSD-1, anchoring them to the membrane in a way which may make the upwards movement required for their activation more difficult. Our results provide insight into how sodium channels are modulated by phosphoinositides, an important step for the development of novel therapies to treat Na_v-related diseases.

Methods

Coarse grained simulations

Coarse-grained simulations of Na_v1.4 embedded in a complex mammalian membrane were carried out to investigate lipid-protein interactions. The inactivated Na_v1.4 alpha subunit (PDB ID: 6agf) (8) was coarse-grained using the CHARMM-GUI Martini Maker (39, 40) and embedded in a 360 Å x 360 Å complex membrane using insane.py (41). The composition of the complex mammalian membrane is as reported in Ingólfsson*, et al.* (42). Three replicate simulations, each with different starting coordinates, were carried out for 16 µs each.

To better sample binding events, we also carried out PIP-enriched simulations in which Na_v1.4 was embedded in a 160 Å x 160 Å POPC membrane with 5% of each PIP species, PIP1, PIP2, PIP3 (with charge parameters of -3e, -5e and -7e respectively), added to the cytoplasmic leaflet using insane.py. Ten replicate simulations, each with different starting coordinates, were carried out for 80 µs each. To validate our proposed binding site, we additionally mutated the positively charged PIP binding site residues K1329, K1330, K1330, K1352, R1460, R1463, K1466 and R1469 to leucines ('8L') or glutamates ('8E) and simulated these mutant channels in enriched PIP membranes for 20 µs in triplicate. To explore the possibility for PIP to stabilize the DIII-IV linker in an inactivation-deficient Nav1.4 variant, additional coarse-grained simulations were carried out where the DIII-IV linker region (residues L1305-K1341) was unrestrained for both the WT Nav1.4 and simulations in which the IFM motif was mutated to IQM. In these simulations, an elastic network was applied to E1314-G1327 in the linker to preserve the helicity of this region. Flexible linker simulations were conducted in triplicate for 20 µs in both PIP-enriched bilayers and POPC-only bilayers.

To explore possible state and subtype dependent differences in PIP binding, the inactivated Na_v1.7 structure (PDB ID: 6j8g) (43) and the Na_v1.7-Na_vPas chimera with CTD bound and VSD-IV in the deactivated state (PDB ID: 6nt4) (14) were also coarse-grained and simulated in PIP-enriched membranes (same protocol as above) for three replicates of 50 µs each. Additionally, a model Na_v1.7 with all four VSDs in the deactivated state was built using Modeller (44) and simulated in triplicate for 50 µs each. The template and structural information for this model are detailed in Table S2. In brief, VSD-I down was modelled from 7xve (45), VSD-II and VSD-III were both modelled from the deactivated VSD-II from 7k48 (46), and VSD-IV and the unbound DIII-IV linker were modelled from the corresponding regions in 6nt4 (14). Adjacent S5/S6 regions to each VSD were also modelled from each specified template to ensure proper contacts between the pore domain and VSDs. The CTD was not included in the model. Using these Na_v1.7 templates, the resting state model of Na_v1.4 was generated and simulated for three replicates in coarse grain with the protein backbone restrained, in a PIP-enriched membrane for 50 µs.

All systems were solvated and ionized with 150 mM NaCl. All coarse-grained simulations were carried out with GROMACS 2022 (47) using the Martini2.2 forcefield (48) and the PIP parameters for each charge

state, where PIP1 is based on PI(3)P and PIP2 is based on PI(3,4)P2 (49). Energy minimization was carried out on each system using the steepest descent method for 1,000 steps. Following this, equilibration in the constant pressure, constant volume (NVT) ensemble at 1 atm for 10 ps was carried out with backbone position restraints (1,000 kJ $mol^{-1}nm^{-2}$) using a 2-fs timestep. Following this, constant pressure and temperature (NPT) equilibration simulations were carried out, using 5-, 10-, and 20-fs timesteps in sequence, with each running for 5,000 steps. 1 atm pressure was maintained using a Berendsen barostat with semi-isotropic conditions. Production simulations were carried out in the NPT ensemble, kept at a temperature of 310 K using the Nose-Hoover thermostat (50) and a pressure of 1 bar using the Parrinello-Rahman barostat (51). A time step of 20 fs was used. During production simulations, the backbone beads were weakly restrained to their starting coordinates using a force constant of 10 kJ $mol^{-1}nm^{-2}$.

Atomistic simulations

Atomistic simulations were performed to characterize atomic interactions between $Na_v1.4$ residues and the bound $PI(4,5)P_2$ headgroup. Frames from a stable PIP2 binding event (from replicate 1 of enriched PIP simulations) were clustered using a selection of the bound PIP2 headgroup beads (C1 C2 C3 PO4 P1 P2) and binding residues K1329, K1330, K1333, K1463, K1466 and R1469 with an RMSD cutoff of 2.5 Å. The protein and bound PIP2 were extracted from the representative frame of the cluster and backbone beads of the coarse-grained VSD-IV were aligned to the corresponding carbon-alpha atoms in the original cryo-EM structure of $Na_v1.4$ (8). PIP2 was backmapped to atomistic coordinates of SAPI24 (the CHARMM lipid for $PI(4,5)P_2$ with -2e charge on P5, -1e charge on P4 and -1e on the PO4, as shown in Fig 4D) and the protein was replaced with the 6agf structure. The system was embedded in a 140 Å x 140 Å POPC membrane, solvated and 0.15 M NaCl added using the CHARMM-GUI Membrane Builder (39, 52, 53). An identical system was set up with $Na_v1.4$ in a POPC membrane without PIP.

Atomistic simulations were performed with Amber20 (54), using the CHARMM36m (55) and TIP3P water (56) forcefields. Equilibration steps were performed (minimization, heating, pressurizing), with 5 kJ/mol restraints on the protein backbone, followed by 24 ns of gradually reducing restraints. Five replicates of unrestrained production equilibrium simulations were performed, run for 1.5 µs each. The temperature was set at 310 K using the Langevin thermostat (57) and at a collision frequency of 5 ps^{-1}. Pressure was set at 1 bar using the Monte Carlo barostat (58) with anisotropic scaling and relaxation time of 1 ps. 12 Å van der Waals cut-off and hydrogen bond SHAKE constraints were used. Hydrogen mass repartitioning was used to enable a 4 fs timestep (59). $PI(4)P_1$ was also simulated with the same atomistic procedures, using the SAPI14 CHARMM lipid (with -2e charge on P4 and -1e on the PO4, as shown in Fig 4D).

Analysis

Coarse grain lipid-protein interactions were characterized using in-house python scripts which used the numpy, MDAnalysis (60) and pandas libraries (as done previously in Lin, Buyan and Corry (61)). A cut-off of 0.7 nm was used to define interactions between lipids and protein residues. Distance heatmaps were generated based on the minimum distance between a PIP bead and the side chain (SC2) bead of the arginine or lysine residue interacting. Binding durations were calculated by first counting the number of interactions between each PIP and VSD-IV binding residues (R1460, R1463, K1466 and R1469). A binding event is defined as the time between the first and last time that PIP interacts with two or more binding residues on VSD-IV, if it interacts with a minimum of one binding residue between this period. Stability of IFM/IQM motif binding in flexible linker coarse-grained simulations was assessed by measuring the distance between the center of mass of the phenylalanine/glutamine residue to the center of mass of three residues (L1153, I1485 and N1591) within the IFM receptor site.

For atomistic simulations, MDAnalysis (60) was used to calculate RMSD of various parts of the protein and PIP headgroup, and RMSF of the carbon-alphas. Statistical significance in RMSF was assessed using student's t-test. ProLIF (62) was used to compute electrostatic interactions between the protein and binding residues. Representative snapshot of PIP2 binding was generated using the WMC Clustering Tool in VMD to identify the top cluster of the PIP2 headgroup (RMSD cutoff of 3 Å), then subsequently cluster the six

binding residues to identify the most representative binding configuration. Trajectories were strided every 1 ns and the first 250 ns of simulations was discarded as equilibration time for analyses of RMSF, ProLIF interactions and clustering. All analysis scripts are available on GitHub.

Simulations were visualized and protein image figures produced using Visual Molecular Dynamics (VMD) (63). ClustalOmega (64, 65) and JalView (66) were used to generate and visualize sequence alignments. Structural representations of $K_v7.1$, $Ca_v2.2$ and $Na_v1.4$ structures were created in VMD by aligning each of the S4 helices on the VSD where the PIP was bound.

Acknowledgements

The authors thank Ruitao Jin for his contributions to the resting state homology model generation and comments on the manuscript draft. This research was undertaken with the assistance of resources and services from the National Computational Infrastructure (NCI), which is supported by the Australian Government. This research is also supported by Australian Government Research Training Program (RTP) Scholarships. Y.L. is supported by a 2023 NCI HPC-AI Talent Program Scholarship.

References

1. F. H. Yu, W. A. Catterall, Overview of the voltage-gated sodium channel family. *Genome biology* **4**, 1-7 (2003).
2. M. Mantegazza, S. Cestèle, W. A. Catterall, Sodium channelopathies of skeletal muscle and brain. *Physiological Reviews* **101**, 1633-1689 (2021).
3. S. L. Venance *et al.*, The primary periodic paralyses: diagnosis, pathogenesis and treatment. *Brain* **129**, 8-17 (2006).
4. K. Jurkat-Rott *et al.*, Voltage-sensor sodium channel mutations cause hypokalemic periodic paralysis type 2 by enhanced inactivation and reduced current. *Proceedings of the National Academy of Sciences* **97**, 9549-9554 (2000).
5. S. D. Dib-Hajj, Y. Yang, J. A. Black, S. G. Waxman, The NaV1. 7 sodium channel: from molecule to man. *Nature Reviews Neuroscience* **14**, 49-62 (2013).
6. M.-R. Ghovanloo *et al.*, Cannabidiol inhibits the skeletal muscle Nav1. 4 by blocking its pore and by altering membrane elasticity. *Journal of General Physiology* **153**, e202012701 (2021).
7. M. de Lera Ruiz, R. L. Kraus, Voltage-Gated Sodium Channels: Structure, Function, Pharmacology, and Clinical Indications. *Journal of Medicinal Chemistry* **58**, 7093-7118 (2015).
8. X. Pan *et al.*, Structure of the human voltage-gated sodium channel Nav1. 4 in complex with β1. *Science* **362**, eaau2486 (2018).
9. T. M. Gamal El-Din, M. J. Lenaeus, N. Zheng, W. A. Catterall, Fenestrations control resting-state block of a voltage-gated sodium channel. *Proceedings of the National Academy of Sciences* **115**, 13111-13116 (2018).
10. S. Raju, A. F. Barber, D. N. LeBard, M. L. Klein, V. Carnevale, Exploring volatile general anesthetic binding to a closed membrane-bound bacterial voltage-gated sodium channel via computation. *PLoS computational biology* **9**, e1003090 (2013).
11. C. Boiteux, I. Vorobyov, T. W. Allen, Ion conduction and conformational flexibility of a bacterial voltage-gated sodium channel. *Proceedings of the National Academy of Sciences* **111**, 3454-3459 (2014).
12. L. J. Martin, B. Corry, Locating the route of entry and binding sites of benzocaine and phenytoin in a bacterial voltage gated sodium channel. *PLoS computational biology* **10**, e1003688 (2014).
13. E. Tao, B. Corry, Characterizing fenestration size in sodium channel subtypes and their accessibility to inhibitors. *Biophysical Journal* **121**, 193-206 (2022).
14. T. Clairfeuille *et al.*, Structural basis of α-scorpion toxin action on Nav channels. *Science* **363**, eaav8573 (2019).

15. A. Cha, P. C. Ruben, A. L. George, E. Fujimoto, F. Bezanilla, Voltage sensors in domains III and IV, but not I and II, are immobilized by Na+ channel fast inactivation. *Neuron* **22**, 73-87 (1999).
16. D. L. Capes, M. P. Goldschen-Ohm, M. Arcisio-Miranda, F. Bezanilla, B. Chanda, Domain IV voltage-sensor movement is both sufficient and rate limiting for fast inactivation in sodium channels. *Journal of General Physiology* **142**, 101-112 (2013).
17. M. P. Goldschen-Ohm, D. L. Capes, K. M. Oelstrom, B. Chanda, Multiple pore conformations driven by asynchronous movements of voltage sensors in a eukaryotic sodium channel. *Nature communications* **4**, 1350 (2013).
18. Z. Yan *et al.*, Structure of the Nav1. 4-β1 complex from electric eel. *Cell* **170**, 470-482. e411 (2017).
19. B. Hille, E. J. Dickson, M. Kruse, O. Vivas, B.-C. Suh, Phosphoinositides regulate ion channels. *Biochimica Et Biophysica Acta (BBA)-Molecular and Cell Biology of Lipids* **1851**, 844-856 (2015).
20. J. Sun, R. MacKinnon, Structural basis of human KCNQ1 modulation and gating. *Cell* **180**, 340-347. e349 (2020).
21. S. Gao, X. Yao, N. Yan, Structure of human Cav2. 2 channel blocked by the painkiller ziconotide. *Nature* **596**, 143-147 (2021).
22. D. Schmidt, Q.-X. Jiang, R. MacKinnon, Phospholipids and the origin of cationic gating charges in voltage sensors. *Nature* **444**, 775-779 (2006).
23. M. A. Kasimova, M. A. Zaydman, J. Cui, M. Tarek, PIP2-dependent coupling is prominent in Kv7. 1 due to weakened interactions between S4-S5 and S6. *Scientific reports* **5**, 1-9 (2015).
24. D. Ma *et al.*, Structural mechanisms for the activation of human cardiac KCNQ1 channel by electro-mechanical coupling enhancers. *Proceedings of the National Academy of Sciences* **119**, e2207067119 (2022).
25. K. D. Gada *et al.*, PI (4, 5) P2 regulates the gating of NaV1. 4 channels. *Journal of General Physiology* **155**, e202213255 (2023).
26. Y. Liu, C. A. Bassetto Jr, B. I. Pinto, F. Bezanilla, A mechanistic reinterpretation of fast inactivation in voltage-gated Na+ channels. *Nature communications* **14**, 5072 (2023).
27. J. C. McPhee, D. S. Ragsdale, T. Scheuer, W. A. Catterall, A critical role for the S4-S5 intracellular loop in domain IV of the sodium channel α-subunit in fast inactivation. *Journal of Biological Chemistry* **273**, 1121-1129 (1998).
28. J. W. West *et al.*, A cluster of hydrophobic amino acid residues required for fast Na (+)-channel inactivation. *Proceedings of the National Academy of Sciences* **89**, 10910-10914 (1992).
29. M. Mantegazza, F. H. Yu, W. A. Catterall, T. Scheuer, Role of the C-terminal domain in inactivation of brain and cardiac sodium channels. *Proceedings of the National Academy of Sciences* **98**, 15348-15353 (2001).
30. F. Bezanilla, C. M. Armstrong, Inactivation of the sodium channel. I. Sodium current experiments. *The Journal of general physiology* **70**, 549 (1977).
31. T. Zaman *et al.*, Mutations in SCN3A cause early infantile epileptic encephalopathy. *Annals of neurology* **83**, 703-717 (2018).
32. A. Frustaci *et al.*, Cardiac histological substrate in patients with clinical phenotype of Brugada syndrome. *Circulation* **112**, 3680-3687 (2005).
33. Y. Liu *et al.*, A PIP2 substitute mediates voltage sensor-pore coupling in KCNQ activation. *Communications biology* **3**, 385 (2020).
34. V. S. Mandala, R. MacKinnon, The membrane electric field regulates the PIP2-binding site to gate the KCNQ1 channel. *Proceedings of the National Academy of Sciences* **120**, e2301985120 (2023).
35. V. Corradi *et al.*, Lipid–protein interactions are unique fingerprints for membrane proteins. *ACS central science* **4**, 709-717 (2018).

36. P. J. Stansfeld, R. Hopkinson, F. M. Ashcroft, M. S. Sansom, PIP2-binding site in Kir channels: definition by multiscale biomolecular simulations. *Biochemistry* **48**, 10926-10933 (2009).
37. P. C. Souza *et al.*, Martini 3: a general purpose force field for coarse-grained molecular dynamics. *Nature methods* **18**, 382-388 (2021).
38. M. Amsalem, C. Poilbout, G. Ferracci, P. Delmas, F. Padilla, Membrane cholesterol depletion as a trigger of Nav1. 9 channel-mediated inflammatory pain. *The EMBO journal* **37**, e97349 (2018).
39. S. Jo, T. Kim, V. G. Iyer, W. Im, CHARMM-GUI: a web-based graphical user interface for CHARMM. *Journal of computational chemistry* **29**, 1859-1865 (2008).
40. Y. Qi *et al.*, CHARMM-GUI martini maker for coarse-grained simulations with the martini force field. *Journal of chemical theory and computation* **11**, 4486-4494 (2015).
41. T. A. Wassenaar, H. I. Ingólfsson, R. A. Bockmann, D. P. Tieleman, S. J. Marrink, Computational lipidomics with insane: a versatile tool for generating custom membranes for molecular simulations. *Journal of chemical theory and computation* **11**, 2144-2155 (2015).
42. H. I. Ingólfsson *et al.*, Lipid organization of the plasma membrane. *Journal of the american chemical society* **136**, 14554-14559 (2014).
43. H. Shen, D. Liu, K. Wu, J. Lei, N. Yan, Structures of human Nav1. 7 channel in complex with auxiliary subunits and animal toxins. *Science* **363**, 1303-1308 (2019).
44. A. Šali, T. L. Blundell, Comparative protein modelling by satisfaction of spatial restraints. *Journal of molecular biology* **234**, 779-815 (1993).
45. G. Huang *et al.*, Unwinding and spiral sliding of S4 and domain rotation of VSD during the electromechanical coupling in Nav1. 7. *Proceedings of the National Academy of Sciences* **119**, e2209164119 (2022).
46. G. Wisedchaisri *et al.*, Structural basis for high-affinity trapping of the NaV1. 7 channel in its resting state by tarantula toxin. *Molecular cell* **81**, 38-48. e34 (2021).
47. P. Bauer, B. Hess, E. Lindahl (2023) GROMACS 2022.5 Manual (2022.5).
48. D. H. de Jong *et al.*, Improved parameters for the martini coarse-grained protein force field. *Journal of chemical theory and computation* **9**, 687-697 (2013).
49. C. A. López, Z. Sovova, F. J. van Eerden, A. H. de Vries, S. J. Marrink, Martini force field parameters for glycolipids. *Journal of chemical theory and computation* **9**, 1694-1708 (2013).
50. D. J. Evans, B. L. Holian, The nose–hoover thermostat. *The Journal of chemical physics* **83**, 4069-4074 (1985).
51. M. Parrinello, A. Rahman, Polymorphic transitions in single crystals: A new molecular dynamics method. *Journal of Applied physics* **52**, 7182-7190 (1981).
52. E. L. Wu *et al.* (2014) CHARMM-GUI membrane builder toward realistic biological membrane simulations. (Wiley Online Library).
53. J. Lee *et al.*, CHARMM-GUI input generator for NAMD, GROMACS, AMBER, OpenMM, and CHARMM/OpenMM simulations using the CHARMM36 additive force field. *Journal of chemical theory and computation* **12**, 405-413 (2016).
54. D. A. Case *et al.* (2020) AMBER 2020. (University of California, San Francisco).
55. J. Huang *et al.*, CHARMM36m: an improved force field for folded and intrinsically disordered proteins. *Nature methods* **14**, 71-73 (2017).
56. W. L. Jorgensen, J. Chandrasekhar, J. D. Madura, R. W. Impey, M. L. Klein, Comparison of simple potential functions for simulating liquid water. *The Journal of chemical physics* **79**, 926-935 (1983).
57. R. J. Loncharich, B. R. Brooks, R. W. Pastor, Langevin dynamics of peptides: The frictional dependence of isomerization rates of N-acetylalanyl-N'-methylamide. *Biopolymers: Original Research on Biomolecules* **32**, 523-535 (1992).

58. J. Åqvist, P. Wennerström, M. Nervall, S. Bjelic, B. O. Brandsdal, Molecular dynamics simulations of water and biomolecules with a Monte Carlo constant pressure algorithm. *Chemical physics letters* **384**, 288-294 (2004).
59. C. W. Hopkins, S. Le Grand, R. C. Walker, A. E. Roitberg, Long-time-step molecular dynamics through hydrogen mass repartitioning. *Journal of chemical theory and computation* **11**, 1864-1874 (2015).
60. N. Michaud-Agrawal, E. J. Denning, T. B. Woolf, O. Beckstein, MDAnalysis: a toolkit for the analysis of molecular dynamics simulations. *Journal of computational chemistry* **32**, 2319-2327 (2011).
61. Y. C. Lin, A. Buyan, B. Corry, Characterizing the lipid fingerprint of the mechanosensitive channel Piezo2. *Biophysical Journal* **121**, 369a (2022).
62. C. Bouysset, S. Fiorucci, ProLIF: a library to encode molecular interactions as fingerprints. *Journal of Cheminformatics* **13**, 1-9 (2021).
63. W. Humphrey, A. Dalke, K. Schulten, VMD: visual molecular dynamics. *Journal of molecular graphics* **14**, 33-38 (1996).
64. M. Goujon *et al.*, A new bioinformatics analysis tools framework at EMBL–EBI. *Nucleic acids research* **38**, W695-W699 (2010).
65. F. Sievers *et al.*, Fast, scalable generation of high-quality protein multiple sequence alignments using Clustal Omega. *Molecular systems biology* **7**, 539 (2011).
66. A. M. Waterhouse, J. B. Procter, D. M. Martin, M. Clamp, G. J. Barton, Jalview Version 2—a multiple sequence alignment editor and analysis workbench. *Bioinformatics* **25**, 1189-1191 (2009).